Pure Appl. Geophys. 168 (2011), 2427–2449

DOI 10.1007/s00024-011-0355-6

Pure and Applied Geophysics

Earthquake Rupture at Focal Depth, Part II: Mechanics of the 2004 M2.2 Earthquake Along the Pretorius Fault, TauTona Mine, South Africa

V. Heesakkers,[1,2] S. Murphy,[3] D. A. Lockner,[4] and Z. Reches[1]

Abstract—We analyze here the rupture mechanics of the 2004, M2.2 earthquake based on our observations and measurements at focal depth (Part I). This event ruptured the Archean Pretorius fault that has been inactive for at least 2 Ga, and was reactivated due to mining operations down to a depth of 3.6 km depth. Thus, it was expected that the Pretorius fault zone will fail similarly to an intact rock body independently of its ancient healed structure. Our analysis reveals a few puzzling features of the M2.2 rupture-zone: (1) the earthquake ruptured four, non-parallel, cataclasite bearing segments of the ancient Pretorius fault-zone; (2) slip occurred almost exclusively along the cataclasite-host rock contacts of the slipping segments; (3) the local in-situ stress field is not favorable to slip along any of these four segments; and (4) the Archean cataclasite is pervasively sintered and cemented to become brittle and strong. To resolve these observations, we conducted rock mechanics experiments on the fault-rocks and host-rocks and found a strong mechanical contrast between the quartzitic cataclasite zones, with elastic-brittle rheology, and the host quartzites, with damage, elastic–plastic rheology. The finite-element modeling of a heterogeneous fault-zone with the measured mechanical contrast indicates that the slip is likely to reactivate the ancient cataclasite-bearing segments, as observed, due to the strong mechanical contrast between the cataclasite and the host quartzitic rock.

1. Introduction

Most of the data on earthquake rupture is determined remotely by seismic and geodetic measurements, and analysis of surface rupture associated with large earthquakes. Direct and near-field observations of rupture-zones at focal depth are rare and limited to deep boreholes and deep mines (McGarr *et al.*, 1979b; Reches and Ito, 2007). The deep gold mines of South Africa offer unique advantages to near-field earthquake studies as the mines provide three-dimensional accessibility to earthquake features within the source region. Our main objective here is to analyze a recent rupture-zone along the Pretorius fault, TauTona mine, South Africa. In Part I (Heesakkers *et al.*, 2011, referred to as Part I), we characterized the structure of the Pretorius fault-zone and the features of the 2004, M2.2 rupture that reactivated this fault-zone. The present study, Part II, focuses on the mechanical analysis of the rupture-zone based on rock mechanics characterization of the fault-rocks, in-situ stress measurements and finite-element modeling of rupture processes.

The reactivation of the Pretorius fault is an expected outcome of the mining around it as in the tectonically inactive region of central South Africa, gold mining is the main source of current seismic activity (Cook, 1963; Spottiswoode and McGarr, 1975; McGarr, 1984; Gibowicz and Kijko, 1994; Mendecki, 1997; Yabe *et al.*, 2009). The mining here is conducted by removal of sub-horizontal layers (reef) of $\sim$1 m thick from a depth of 1.5 to 3.5 km for gold extraction. This operation is conducted in regions that are hundreds of square kilometers in size. The downward motion of the overburden into the removed reef space releases gravitational energy of 10^{13}–4×10^{14} J for each square kilometer of mined area. This released gravitation energy is accommodated by three types of processes: (a) intense fracturing and fresh rock faulting at the propagating mining face; (b) aseismic bending of the overburden into the removed reef space; and (c) reactivation of existing, usually ancient, fault-zones. The majority of mining-induced earthquakes belong to group (a): they are spatially located close to the advancing mine face (Gay and Ortlepp, 1979), and temporally associated with the mining explosions

[1] School of Geology and Geophysics, University of Oklahoma, Norman, OK, USA. E-mail: reches@ou.edu
[2] *Present Address*: Chevron ETC, 1500 Louisiana St, Houston, TX 77002, USA.
[3] AngloGold Ashanti, Carletonville, South Africa.
[4] US Geological Survey, 345 Middlefield Rd MS977, Menlo Park, CA 94025, USA.

(MENDECKI, 1997). These events often involve coseismic volume reduction in addition to fault slip, and are thus interpreted as the interaction between faulting and the closure of nearby mine opening (MCGARR, 1992; RICHARDSON and JORDAN, 2002).

Recognizing earthquakes of group (c) is more complicated (RICHARDSON and JORDAN, 2002; YABE *et al.*, 2009). To identify them, BOETTCHER *et al.* (2009) examined the seismic data of 12 years in TauTona mine (Part I, Fig. 1) and analyzed the events that occurred during hours or days without mining operations. They found that these "…mining-induced earthquakes follow the Gutenberg–Richter relation with no scale break down to the completeness level of the catalog, at moment magnitude M_W −1.3. Events recorded during relatively quiet hours in 2006 indicate that catalog detection limitations, not earthquake source physics, controlled the previously reported minimum magnitude in this mine." YABE *et al.* (2009) used a local network of acoustic emission (AE) sensors to analyze the earthquake rupture of at depth of 3.3 km in Mponeng gold mine, close to TauTona mine, South Africa (Part I). Their system monitored a 30-m thick dyke that failed by a M1.9 event due to mining. The more than 13,000 well located AE events recorded during the 150 h after the main event delineate a distinct quasi-planar cluster of ∼100 × 80 m around the M1.9 hypocenter. YABE *et al.* (2009) interpreted this cluster as the aftershocks that followed the M1.9 earthquake. These

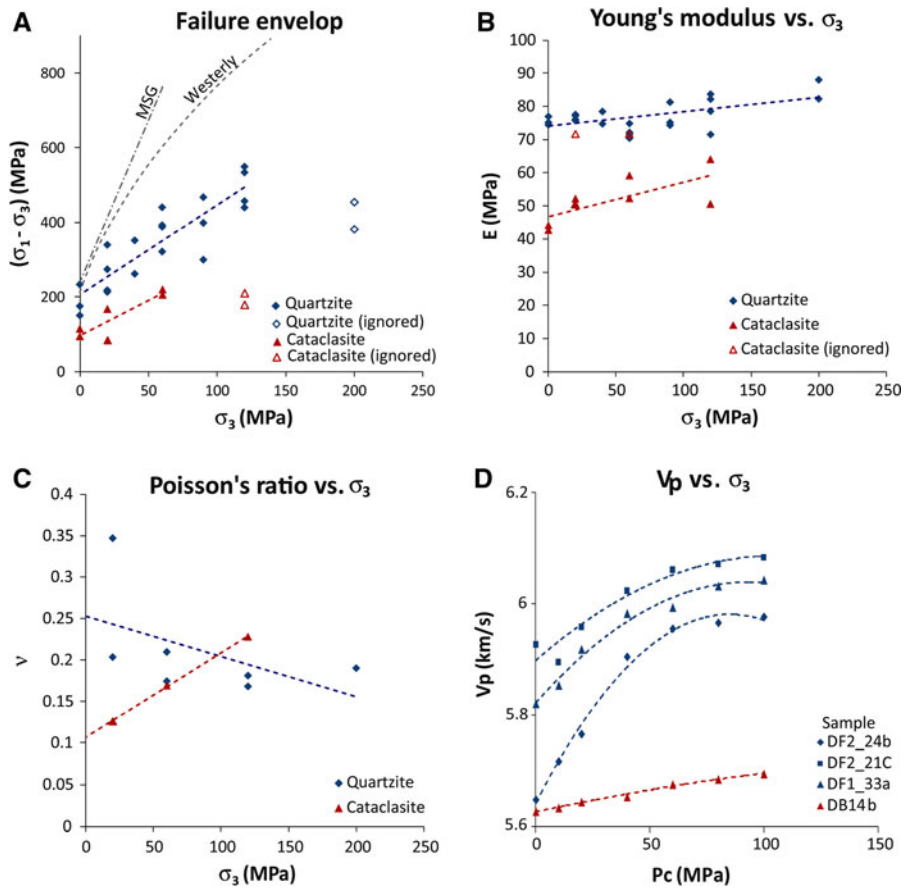

Figure 1

Rock-mechanics experimental results for the Pretorius fault-zone. **a** Differential stress at failure versus confining pressure; quartzite-blue dots, cataclasite-red dots, with linear regression fit; the linear regression lines do not include results of high confining pressure runs (200 MPa for quartzite and 120 MPa for cataclasite). Also shown: the failure envelopes for Mount Scott granite (MSG) after KATZ *et al.* (2001), and Westerly granite (Westerly) after LOCKNER (1998). **b** Young's modulus (*E*) versus confining pressure. **c** Poisson's ratio versus confining pressure (see text). **d** P-wave velocities (*blue dots*) versus confining pressure (text for details)

observations suggest that even though mining-induced earthquakes are activated by mining stresses, the physical processes of these events is similar to earthquakes along faults activated by tectonic loading.

Mining-induced earthquakes along existing fault-zones provide a rare research opportunity. The 3D rupture-zones of these events can be studied at focal depth for small events, whereas rupture-zones of large tectonic earthquakes are accessible only at the earth surface, exposed in two-dimensions, and are highly modified by soil properties and surface waves.

2. *Rupture-Zones of Earthquakes at Focal Depth*

The first detailed analysis of the rupture-zone of an earthquake in a mine was conducted in South African East Rand Proprietary Mines through a system of passages mined into the zone (Gay and Ortlepp, 1979, Ortlepp, 1978; Spottiswoode, 1980; McGarr *et al.*, 1979a). They found two fault-zones with areas of 500 and 600 m^2 and typical offsets of 0.06 m that cut previously intact quartzite and generated a structure spanning over several orders of length scales. McGarr (2002) attributed this rupture-zone to a reported event with moment magnitude of 3.8; this interpretation is based primarily on the observed maximum slip of 0.1 m. The expected source area of such event should approach 10^6 m^2 in contrast to the observed areas of 500 and 600 m^2. Thus, it seems that the energy of this event represents intense rupture and fragmentation within the fault volume. Comprehensive, high resolution, near-field monitoring of earthquakes in the deep mines has been conducted since 1994 by Japanese and Japanese-German groups led by Hiroshi Ogasawara (Ogasawara, 2002; Yabe *et al.*, 2009).

Recent earthquake rupture studies in the deep mines focused on the rupture-zones associated with large earthquakes that developed by slip along existing faults (Dor *et al.*, 2001; van Aswegen *et al.,* 2002). The April 22, 1999, $M = 4.6$ Matjhabeng earthquake in Welkom area was one of the largest mining-induced earthquake in South Africa, and it was the last in a series of three earthquakes with M4.0 since 1976 along the Dagbreek fault. This event, mapped in three tunnels at 1,660 m below surface, displaced rail tracks within a tunnel for 44 cm vertically (Dor *et al.*, 2001). Displaced rock bolts were found at distances of 30–45 m from the main slip surface of the Dagbreek fault, showing the width of the rupture-zone. This zone is characterized by several fine grained and/or clayey, soft fresh gouge zones of 0.5–5 cm thick that characterize individual slip surfaces of the M4.6 rupture.

Most faults in the Witwatersrand basin, including the Pretorius fault, have not slipped in at least several hundred million years and perhaps billions of years. The Natural Earthquakes Laboratory in South African Mines (NELSAM) project was designed to study earthquake processes at their focal depths (Reches, 2006; Part I). The main site of the project is located around the Pretorius fault within the TauTona mine. We analyze here the rupture-zone of the M2.2 event of December 12, 2004, that is exposed within a few tunnels in the TauTona mine at a depth of 3.6 km. This event, described in Part I, reactivated several quasi-planar segments of the Pretorius fault-zone that formed $\sim$2.7 Ga ago and has been inactive during the last 2.0 Ga. We analyze here a few central aspects of this event. First, the mechanical properties of the fault zone are determined by rock mechanics experiments. Second, the stress field associated with the M2.2 event is determined from borehole breakouts. Finally, we used the measured mechanical heterogeneities within the fault zone to model the reactivation processes with finite element simulations.

3. *Mechanical Properties of the Pretorius Fault Zone*

The mechanical properties of the Pretorius fault-rocks were determined experimentally. We used only core samples that were collected from boreholes which are not damaged by blasting. Samples were collected from three boreholes within the Pretorius fault-zone, DafBio, Daf1 and Daf2 (Part I, Fig. 3) that were drilled sub-parallel to bedding surfaces that locally dip $\sim$22° to the south. The collected samples of the quartzitic host rock contain delicate bedding features that are recognized by grain size differences and pyrite rich beds, which are oriented sub-parallel

to the sample axis. The cataclasite samples were taken from DafBio and some of them contain a partly developed foliation oriented 20°–30° to the sample axis. This foliation orientation, which was dictated by the core inclination, is favorable for shear failure under triaxial loading in which σ_1 parallels the sample axis (Reches, 1979). Therefore, the strength values, and probably the Young modulus, that are derived below represent the lower end of the cataclasite strength. We measured strength, elastic parameters and acoustic velocities under confining pressures up to 200 MPa. Tests were conducted in the rock-mechanics lab of the USGS in Menlo Park, CA.

3.1. Sample Preparation and Experimental Setup

A set of 22 host-rock quartzite samples and 8 cataclasite samples were tested. The quartzite cores were re-drilled to 75 mm long samples, 25 mm in diameter. The more brittle cataclasite samples were cut into rectangular prisms of 55 × 18 × 18 mm. A two component strain gage was mounted on seven quartzite samples and three cataclasite samples. The quartzite samples were jacketed with a polyurethane jacket, and the cataclasite samples were jacketed with heat shrink plastic.

The experiments were conducted in a standard non servo-controlled triaxial test apparatus with oil confining medium, external load cell and under room-dry conditions at room temperature. Sixteen quartzite experiments were run, with duplicates, at 0, 20, 60, 90, 120 and 200 MPa confining pressure, and five cataclasite experiments were run at 0, 20, 60 and 120 MPa confining pressure. Strain gages were used on both rock types samples at 20, 60, 120 and 200 MPa confining pressure. An axial strain-rate of 3×10^{-6} s^{-1} was typically applied by an axial piston velocity of 0.2 μm/s. All these experiments were carried out to failure. Six additional quartzite experiments were continued to a total piston displacement of 5 and 10 mm to initiate sliding on the failure zone. Three additional sliding experiments with 5 mm piston displacement were conducted on the cataclasite samples. The conditions and main results are listed in Table 1. Poisson's ratio was determined for experiments with strain gages.

3.2. Results

3.2.1 Strength

The maximum differential stress, $d\sigma_u = \sigma_1 - \sigma_3$, increases linearly with confining pressure (Fig. 1a) in agreement with a Mohr–Coulomb failure criterion. The strength of samples loaded under the highest confining pressure, 200 MPa for the quartzite and 120 MPa for the cataclasite, deviate from linearity (Fig. 1a), and are not incorporated in the strength linear regression. The mean uniaxial strength is 207 MPa for the quartzite (three samples), and 99 MPa for the cataclasite (two samples). For comparison, the strength of Mount Scott granite (Katz *et al.,* 2001) and Westerly granite (Lockner, 1998) are displayed in Fig. 1a. We use the Coulomb failure criterion,

$$\tau = C + \sigma_n \tan \varphi$$

where τ and σ_n are the shear stress and the normal stress on the fault plane, C is cohesion, and φ, is the angle of internal friction. The calculated values for the quartzite are $C = 49$ MPa and $\varphi = 39°$, and for the cataclasite $C = 29$ MPa and $\varphi = 29°$.

3.2.2 Elastic Properties

Young's modulus (Fig. 1b) is calculated from the strain gage readings, and from load cell readings, corrected for machine stiffness in experiments without strain gages. Young's modulus gently increases linearly with confining pressure. The two data points for the cataclasite at confining pressures of 20 and 60 MPa (Nel35 and Nel36, Table 1) are not included in the linear relation due to jacket oil leak during these experiments. The Young's modulus for quartzite and cataclasite is 77 ± 6.3 and 52 ± 5.7 GPa, respectively. The quartzite Poisson's ratio is 0.21 ± 0.06 with one outlier at 20 MPa confining pressure (Fig. 1c). The cataclasite Poisson's ratio is 0.23 based on one sample (jacket oil leak in the other two runs with strain-gages).

3.2.3 P-Wave Velocity

P-wave velocities were measured in three quartzite samples that were 25 mm in diameter and 25 mm

Table 1

Conditions and results for rock mechanics experiments

Run	Sample	P_C (MPa)	Peak strength ($\sigma_1 - \sigma_3$) (MPa)	Young's modulus (GPa)	Poisson's
A. Quartzite within the Pretorius fault					
Nel24	DF2_23Bb	0	174.7	76.9	
Nel07	DB13b	0	149.6	74.4	
Nel01	DF2_23Aa	0	232.7	75.1	
Nel29	DF2_21b	20	212.7	76	
Nel31	DB18a	20	217	77.5	
Nel08	DF1_33b	20	338.9	77.1	0.20
Nel09	DF2_24a	20	273.3	75.7	0.35
Nel11	DF1_31Aa	40	261.1	74.7	
Nel10	DF2_23c	40	350.8	78.4	
Nel23	DB12b	60	440.3	74.8	0.17
Nel13	DF2_23Aa	60	387.4	70.4	0.21
Nel16	DF1_32Bb	60	320.8	72.1	
Nel14	DF1_31B	60	392.3	71.6	
Nel15	DF1_31Ab	90	467.5	75.1	
Nel17	DF2_26a	90	299	74.3	
Nel22	DF2_21c	90	298.5	81.2	
Nel21	DF1_32Aa	120	534	78.5	
Nel19	DB13a	120	457	83.6	0.17
Nel18	DB11	120	549.3	82.1	0.18
Nel20	DF2_22a	120	439.7	71.5	
Nel27	DF2_26b	200	453.9	87.9	0.19
Nel28	DF1_32Ab	200	380.8	82.2	
Run	Sample	P_C (MPa)	Peak strength ($\sigma_1 - \sigma_2$) (MPa)	Youngs modulus (GPa)	Poisson's
B. Cataclasite					
Nel32	DB50Bb2	0	95.1	42.6	
Nel34	DB14Aa2	0	115	44.1	
Nel39	DB50Ba2	20	167.9	52.2	
Nel35	DB14Aa1	20	83.9	71.7	0.13
Nel40	DB14Ab1	60	219.9	52.3	
Nel36	DB50Bb1	60	205.8	71.7	0.17
Nel41	DB14Ab2	120	209.2	50.6	
Nel38	DB50Ba1	120	178.1	64.1	0.23

long, and in one cubic cataclasite sample 25 mm on side. All the samples were derived from the same cores as the rock mechanics experiment samples, all from within the Pretorius fault-zone. The first arrivals of a voltage pulse at 10 MHz were measured at confining pressures of 10, 20, 40, 60, 80 and 100 MPa, using an oscilloscope.

The V_P of the quartzite increases significantly with confining pressure, from as low as 5.64 km/s to maximum values of 5.98–6.08 km/s (Fig. 1d). This increase of V_P suggests wide-spread crack closure within the samples. The cataclastic sample displays only minor increase of V_P with increasing confining pressure, suggesting negligible crack closure; the maximum V_P for the cataclasite is 5.69 km/s.

3.3. Damage Analysis

The increase in V_P with increasing confining pressure in the quartzite was the first indication that the quartzite is internally damaged. We determine the inelastic strain for the seven experiments with strain gages by subtracting the calculated elastic strain from the total measured strain following KATZ and RECHES (2004). Considering the Poisson's effect and Hooke's law, the axial elastic strain, $(\varepsilon_{zz})_{elast}$, and the

circumferential elastic strain, $(\varepsilon_{xx})_{\text{elast}}$, can be calculated from the following relationships:

$$(\varepsilon_{zz})_{\text{elast}} = \frac{1}{E}\left[\sigma_{zz} - \nu\left(\sigma_{xx} + \sigma_{yy}\right)\right]$$

$$(\varepsilon_{xx})_{\text{elast}} = \frac{1}{E}\left[\sigma_{xx} - \nu\left(\sigma_{yy} + \sigma_{zz}\right)\right]$$

where E and ν are the Young's modulus and Poisson's ratio, respectively, as derived above from the linear part of the stress/strain curve. For rock mechanics experiments under constant confining pressure, σ_{xx} and σ_{yy}, which are initially loaded and held constant during the deformation, may be subtracted, and thus reduces the above equations to (KATZ and RECHES, 2004):

$$(\varepsilon_{zz})_{\text{elast}} = \frac{\sigma_{zz}}{E}$$

$$(\varepsilon_{xx})_{\text{elast}} = -\frac{\nu\sigma_{zz}}{E}$$

The inelastic strain, $(\varepsilon)_{\text{inelast}}$, is calculated by subtracting the elastic strain, $(\varepsilon)_{\text{elast}}$, from the total experimental strain following the method of KATZ and RECHES (2004):

$$(\varepsilon_{zz})_{\text{inelast}} = (\varepsilon_{zz})_{\text{total}} - (\varepsilon_{zz})_{\text{elast}}$$

$$(\varepsilon_{xx})_{\text{inelast}} = (\varepsilon_{xx})_{\text{total}} - (\varepsilon_{xx})_{\text{elast}}$$

The inelastic strain curves of the seven quartzite samples are shown in Fig. 2. Negative strain on the right represents the axial strain ε_{zz}, positive strain on the left represents the circumferential strain ε_{xx}. The axial and circumferential elastic strains are also illustrated by the dashed lines. The axial inelastic strain is generally smaller than the elastic strain, with maximum values up to 0.8% for high confining pressures. The circumferential inelastic strain reaches strains >1% for high confining pressures, significantly larger than the circumferential elastic strain of <0.4%. This observation suggests significant damage of the quartzite samples before failure, by dilation, along axis-parallel micro-fractures.

The damage of the samples was further quantified by evaluating the deformation modulus, which is the local slope of the stress–strain curve (KATZ and RECHES, 2004). Figure 3a, b illustrates the axial and volumetric strain curves for experiments on quartzite (sample Nel08) and cataclasite (sample Nel35), both under 20 MPa confining pressure. The quartzite

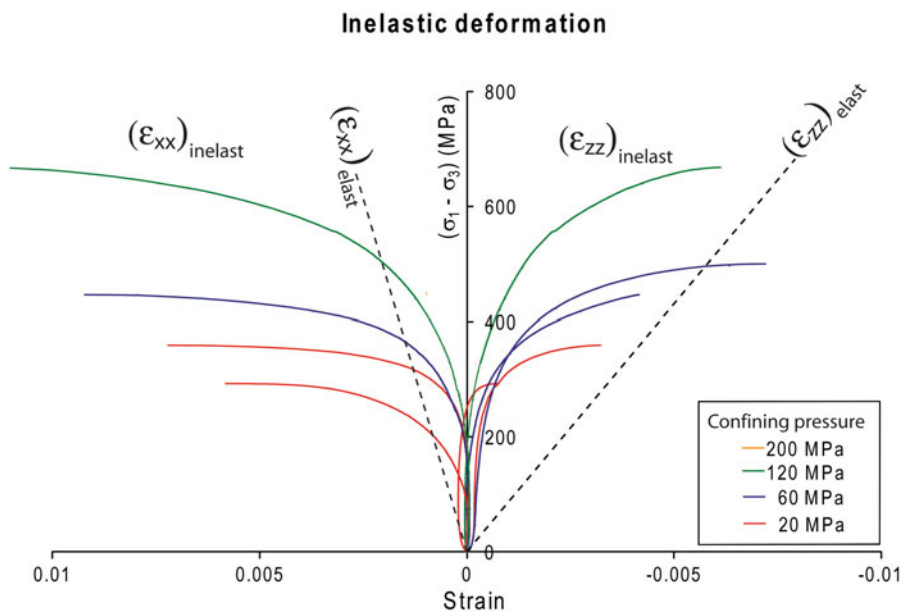

Figure 2

Deformation in seven quartzite samples tests (see text). The right side displays the inelastic axial strain $\varepsilon_{zz(\text{inelactic})}$ versus differential stress; the left side displays the inelastic circumferential strain $\varepsilon_{xx(\text{inelastic})}$ (positive); *dashed lines* are the elastic strain. Note that the axial inelastic strains are generally smaller than the axial elastic strain, whereas the circumferential inelastic strains are significantly larger than the circumferential elastic strains

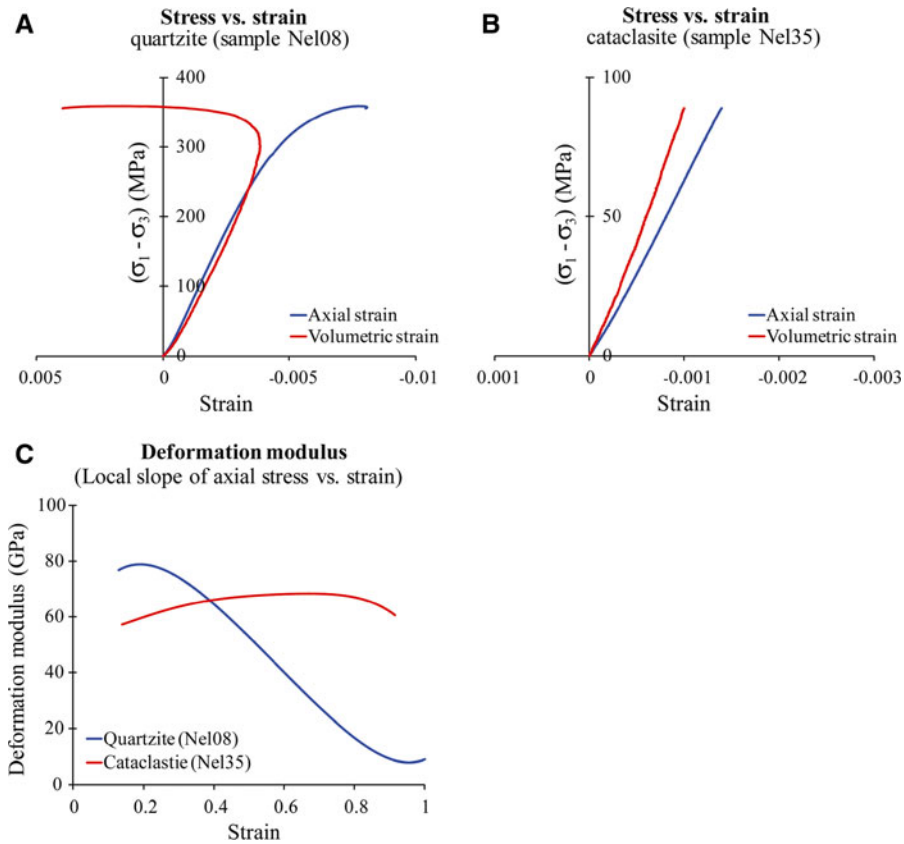

Figure 3
Characteristic stress–strain curves for confining pressure of 20 MPa. **a** Quartzite sample Nel08; note strain hardening before failure with significant volumetric strain (*red*) into the extensional (positive) strain field. **b** Cataclasite sample Nel35; note linear elastic behavior without strain hardening and only minor volumetric strain (compressive); note scale difference from **a**. **c** Deformation modulus calculated for **a** and **b** (see text). Note that the deformation modulus for the quartzite decreases from 80 to 10 GPa with increasing strain, starting at ~20% of the total strain, whereas the deformation modulus of the cataclasite decreases only slightly

samples undergo significant strain-hardening before failure with significant volumetric strain into the extensional strain field. The cataclasite behaves linearly elastic without significant strain hardening or volumetric strain, with failure occurring at significant lower strains and stresses (note the scale difference in Fig. 3).

Figure 3c displays the deformation modulus for both rock types as a function of the normalized strain (with respect to strain at failure). The deformation modulus of the quartzite decreases significantly after 20% of the normalized strain, with values dropping from ~80 GPa to below 10 GPa. This trend of the deformation modulus is similar to the behavior of Mount Scott granite described by KATZ and RECHES (2004), who showed that this damage is associated with formation and dilation of micro-fractures. The deformation modulus of the cataclasite decreases only slightly with increasing strain, indicating that it behaves more brittle with less damage, with respect to the stronger and more damaged quartzite.

The extensive damage in the quartzite and its relation to the formation of micro-fractures is further examined in analysis of thin sections made of samples for both rock types that failed under 20 MPa confining pressure (Fig. 4). The main fault within the quartzite samples (red arrow in Fig. 4) consists of up to 0.35 mm wide cataclastic zone with angular clasts up to 0.2 mm within a very fine grained matrix. The blue epoxy, penetrating dilatant fractures away from the main fault, indicates significant off-fault damage. The damage is characterized by fault-parallel branches that terminate at axial fractures within quartz grains. The axial fractures are most

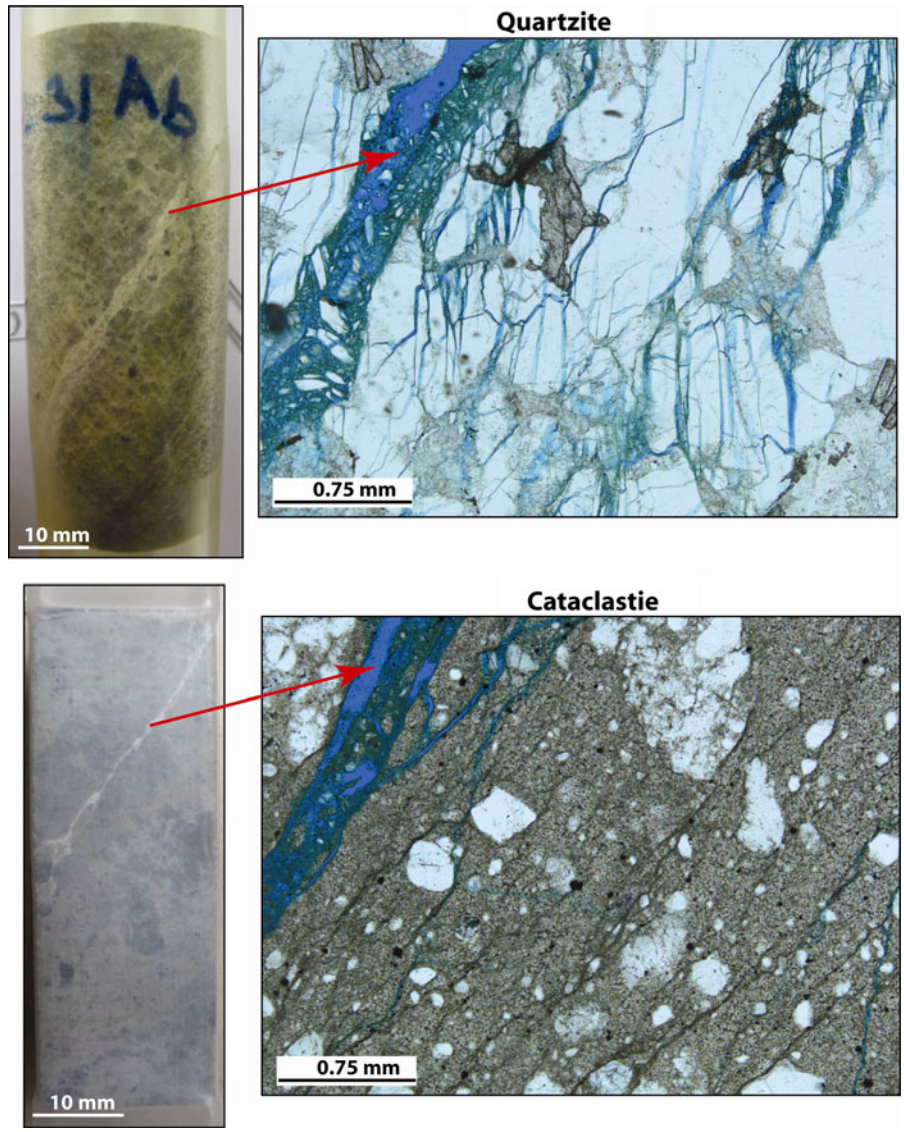

Figure 4
Thin-sections of the experimental fault-zones in runs under 20 MPa confining pressure. Dilated areas are filled with blue epoxy. Note extensive off-fault damage in the quartzite dominated by micro-fractures that branch from the main fault and die away from it, and multiple axial fractures within quartz grains away from the fault. The cataclasite displays a narrow fault that developed parallel to the matrix foliation, only minor off-fault damage

abundant near the major fault, and become less abundant further away from the main fault. Most axial fractures do not propagate past grain boundaries of individual quartz grains. We interpret the axial fractures to have nucleated at preexisting micro-flaws within internally damaged quartz grains. The axial fractures propagate during loading, contributing to the strain-hardening and volumetric expansion of the sample.

In the experiments, the fault within the cataclasite samples forms a narrow fault zone up to 0.2 mm wide, with minor off-fault branching. No significant damage is observed away from this fault (no blue epoxy), in contrast to the fault in the quartzitic host-rock samples (Fig. 4). Quartz grains within the matrix of the cataclasite remain intact. Note that the main fault formed parallel to the poorly developed foliation within the cataclasite.

3.4. Mechanically Heterogeneous Fault-Zone

The most striking result of our rock mechanics experiments is the contrasting mechanical properties of the quartzitic host rocks and the cataclasite (Figs. 1, 3, 4; Table 2). As both the host rock and cataclasite are essentially identical mineralogically, the mechanical contrast could stem from two textural factors. First, the host rocks are coarse grained with grain size of 1–3 mm, whereas the cataclasite is composed of 0.5–1 mm grains embedded in very fine grain matrix with sub-micron size (Fig. 4). Upon loading, the large grains of the host rock develop a dense network of microcracks, whereas the large grains in the cataclasite remain uncracked (Fig. 4). Second, the host rock has no foliation, whereas the cataclasite may have a weak foliation and it failed parallel to the foliation (Fig. 4). As the orientation of the cataclasite samples was dictated by the core orientation (above), we could not test systematically the strength as function of foliation orientation. We think that the influence of the second factor (foliation strength) is smaller than the first factor (grain-size, damage), based on a sample with preserved contact between cataclasite without foliation and host rock (Fig. 11 below and related discussion). This mechanical contrast represents the heterogeneous nature of the Pretorius fault, and we use this contrast to model and explain the recent rupture by an M2.2 event along the Pretorius fault.

4. The 2004, M2.2 Event in TauTona Mine

4.1. The Pretorius Fault-Zone

The study area is in the TauTona mine that is located in the Western Deep Levels of the Witwatersrand Basin, South Africa (Part I, Fig. 1). This basin consists of about 10 km thick sequence of sedimentary rocks, mainly sandstones, mudrocks, and gold-bearing conglomerates (Armstrong *et al.*, 1991; Gibson *et al.*, 2000; Robb *et al.*, 1997). The basin underwent low-grade metamorphism and was tectonically inactive for the last 2.5 Ga (Robb *et al.*, 1997). The Pretorius fault is a ~10 km long, oblique strike slip fault with oblique displacement of up to 200 m. The structure of the Pretorius fault-zone indicates that during its Archaean activity times, it entered the stage of slip localization with multiple events localized along a single principal slip zone (Part I). We identified three structural zones within the Pretorius fault-zone (Fig. 5):

1. An outer damage zone, ~100 m wide, of brittle deformation manifested by multiple widely spaced fractures and faults with slip up to 3 m (Fig. 5b).
2. A inner damage zone, 25–30 m wide, with high density of anastomosing conjugate set of moderate to steeply dipping (40°–90°) fault segments, with quasi-planar surfaces that crosscut, intersect and branch from each other; many of these segments carry cataclasite zones (Fig. 5c). Bedding-parallel fault surfaces that dip ~22° also occur in the northern side of this zone.
3. A single, dominant segment, with a cataclasite zone up to 0.5 m thick, is the principal slip zone that accommodated most of the slip of the Pretorius fault (Fig. 5c, Part I, Fig. 8).

Many of the segments carry cataclasite zones that vary in thickness from a few millimeters to tens of centimeters (Part I, Fig. 8). The cataclasite is a cohesive, green to gray quartzitic rock with a wide range of grain size distribution: coarse and angular to rounded quartzite clasts, 1 mm–20 cm in size, which are supported by an ultra-fine quartzitic matrix (Part I). Abundant flow features on macro- and micro-scale consist of injection veins and flow banding. We showed that the cohesive cataclasite formed by sintering of granular material (Part I).

The 2004 M2.2 earthquake reactivated at least four non-parallel segments of the ancient Pretorius fault, one of which includes the PSZ, at 3.6 km depth (Part I). We located and mapped the rupture-zone of the M2.2 event and showed that (Part I) (1) slip occurred almost exclusively along four pre-existing,

Table 2

Summary of mechanical rock properties of Pretorius fault

	E	ν	U_s	(C, μ_i)	Brittleness	Damage
Host rock	77	0.21	207	49, 0.81	Brittle-plastic	Intense
Cataclasite	52	0.23	99	29, 0.55	Brittle-elastic	Minor

E Young's modulus (GPa), ν Poisson's ratio, U_s uniaxial strength (MPa), C Coulomb criterion cohesion, μ_i coefficient of internal friction

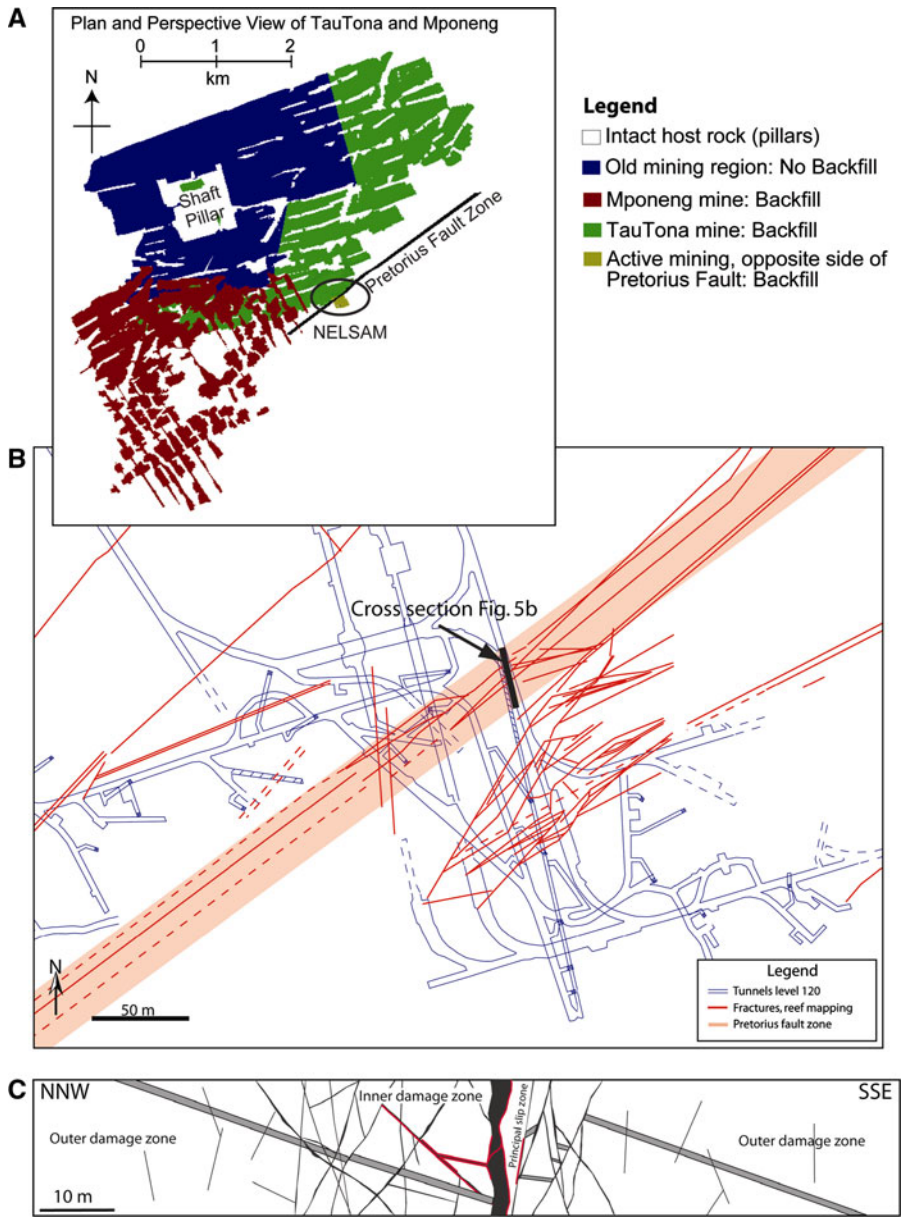

Figure 5

Structure of the Pretorius fault-zone. **a** Plan view of the mining at Mponeng mine (*brown*) and TauTona mine (*blue* and *green*) and the Pretorius fault (*black*) (after Lucier *et al.*, 2009). The colored regions are mined areas, and the uncolored regions are un-mined, intact rock left as pillars. The NELSAM research site is marked in the southeastern part of TauTona mine. **b** Fault and fracture map of the mined reefs in the NELSAM site prepared and provided by the geology team of TauTona mine. The fault traces are projected on top of the tunnel network of level 120 (*blue*). **c** A generalized cross-section of the Pretorius fault-zone that is based on the tunnel map in 118-xcut tunnel (Part I). Note the density of multiple branching segments, the development of a $\sim$1 m thick principal slip zone (PSZ) that accumulated most of the slip along the Pretorius fault and separates the bedding-surface rich northern block from the southern block (details in Part I)

large, quasi-planer segments of the ancient fault-zone; (2) the slipping segments contain brittle cataclasite zones up to 0.5 m thick; (3) these segments are not parallel to each other; (4) gouge zones, 1–5 mm thick, composed of white 'rock-flour' formed almost exclusively along the cataclasite-host rock contacts of the slipping segments; (5) locally, new, fresh fractures branched from the slipping

segments and propagated in mixed shear-tensile mode; (6) the maximum observed shear displacement is 25 mm in oblique-normal slip.

4.2. In-Situ Stresses

4.2.1 Approach

The perturbations of the in-situ stress field by large scale mining activities at depths are the main source for seismic activity in the mines. The M2.2 rupture is located within an area of an elaborate tunnel networks, and ~20 m below the mined reef. Determination of the in-situ stress at this region of the TauTona mine was a major undertaking of the NELSAM project (Lucier *et al.,* 2009). Our in-situ stress analysis is based on breakout observations in 12 boreholes and boundary element modeling (Lucier *et al.,* 2009). The boreholes were logged with a slim borehole Digital Optical Televiewer made by Robertson Geologging, UK. Eight of the boreholes are 10 m deep, located within or close to the Pretorius fault-zone, three of which as close as 60 m from the M2.2 rupture-zone (holes 10, 13 and 9 in Fig. 6). All these boreholes are 75 mm in diameter. The fractures observed in these boreholes were analyzed in Part I. The far field (regional) in-situ stress around TauTona mine is based on logging a separate, sub-horizontal borehole at the margins of the TauTona mine (Fig. 6).

4.2.2 Far Field Stress State

The Witwatersrand Basin forms part of the cratonic crust of South Africa. McGarr and Gay (1978) showed that the crust in South Africa is under a normal faulting regime such that $S_V \geq S_{Hmax} \geq S_{hmin}$. In-situ stress measurements were conducted in the shaft pillar of TauTona mine at a depth of 2,361 m using overcoring technique (Cartwright and Walker, 2000). They found that the maximum compressive stress (σ_1) deviates 20° from vertical and plunges to the NNW. The intermediate principal stress (σ_2) deviated 20° from horizontal in the SSE direction with a vertical gradient of 19 MPa/km. The minimum principal stress (σ_3) was nearly horizontal in the WSW direction with a vertical gradient of 10 MPa/km.

As part of the NELSAM project, we determined the far field in-situ stresses in the area that is likely to be unaffected by mining operations (Lucier *et al.,* 2009). For this purpose, we logged a 418 m sub-horizontal borehole that was drilled at a depth of 3.5 km, away from the active mining area (LIC118 borehole in Fig. 6). This borehole trends generally to the east, and deviates up to 15° from horizontality.

Lucier *et al.* (2009) identified multiple breakouts from borehole distance 35 m throughout the entire length of the borehole (Fig. 7). They recognized four zones each with uniform breakout orientation and width. The deepest zone from 150 to 418 m displays

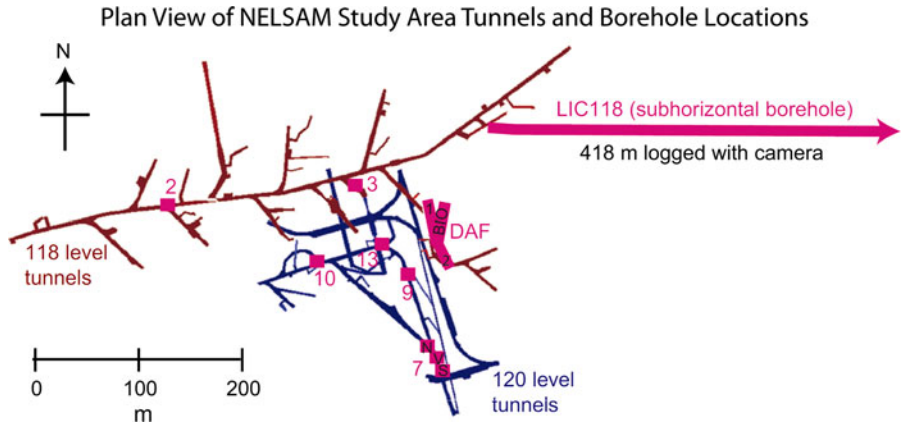

Figure 6

Map view of borehole locations and tunnels in the NELSAM site (Part I), TauTona mine (from Lucier *et al.*, 2009). Tunnels of level 118 (*red*) and level 120 (*blue*) are projected on top of each other. The currently mined area dips 20°–25° to the SSE. Site 2 and 3 are vertical boreholes at level 118, site 6, 7 V, 9, 10 and 13 are vertical boreholes at level 120, and the sub-horizontal exploration hole LIC118 at level 118

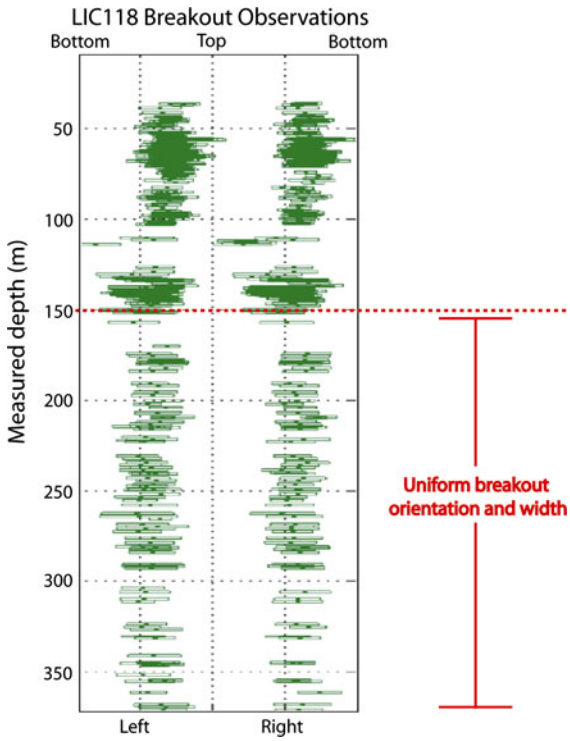

Figure 7
Borehole breakouts marked by *green rectangles* observed in 418 m of borehole image of LIC118 (location in Fig. 6) (from Lucier *et al*., 2009). Borehole breakouts are observed from 35 m depth and continue to the entire logged borehole. Note that after 150 m depth the breakouts maintain constant orientation and width that indicate the far-field stress-state (text)

constant breakout orientation and width, and this consistency away from the mine tunnels was interpreted as indicating the far field stress (Lucier *et al.*, 2009). The stress state determined for the breakouts in the 150–418 m interval was further constrained by an iterative forward modeling with the boundary element program Map3D (Lucier *et al.*, 2009). The modeling examined the possible perturbation by the mining geometry and its timing on the stresses in the logged borehole. This analysis yielded a well constrained far-field stress state with the maximum compressive stress (σ_1) deviated 0–20° from vertical, plunging towards the NNW and a magnitude gradient of 26.7–27.3 MPa/km, an intermediate principal stress (σ_2) inclined 0–20° towards 157–168° with magnitude gradient of 21–26 MPa/km, and least compressive stress (σ_3) inclined 0–10° towards 235–258°, with magnitude gradient of 12.9–15.5 MPa/km (Fig. 8). This stress state is of normal faulting regime as suggested by McGarr and Gay (1978), with principal stress orientations similar to those determined by Cartwright and Walker (2000) in the shaft pillar (above).

4.2.3 Stress State Close to the Rupture-Zone

We determined the in-situ stress state at the proximity of the M2.2 event from breakouts observed in three boreholes located within 60 m horizontally and 15 m vertically from the exposed rupture-zone (holes 10, 13 and 9 in Fig. 6). These boreholes are up to 11.5 m deep with a diameter of 75 mm and vertical deviations up to 1.5°. Clear stress indicators are observed within holes 10 and 13, whereas hole 9 did not reveal any breakouts.

The images of borehole 13 reveal several zones of well developed breakouts with cumulative length of 2.87 m (Fig. 9a). The breakouts are continuous, accompanied by significant spalling, displaying width of 32–40°, and terminating abruptly against fault-zones and bedding surfaces. The images of borehole 10 reveal breakout zones with cumulative length of 2.6 m out of 10.02 m logged depth (Fig. 9b). Most of these breakouts are in the incipient stage of failure: they are partly discontinuous, and show minor spalling with widths of only a few degrees to $\sim$20°. Yet, these breakouts have the distinct features of breakouts: $\sim$180° between the two sides, consistent trends in the borehole, and abrupt termination against faults (BO in Fig. 9b). The mean orientation of the 11 clear breakout zones in both boreholes is 243.5° $\pm$ 7.7° that indicates S_{Hmax} trend of 333.5° $\pm$ 7.7°.

Borehole 10 also includes drilling-induced tensile fractures (DITF) that complement the breakout zones. One DITF is about 1 m tall and centered at a depth of about 9.1 m below the tunnel floor (DITF_A in Fig. 9b). It appears as a narrow, dark vertical (axial) feature, bisecting the interval between the breakouts and limited to one block with its two traces at 184° to each other. This appearance corresponds to an axial DITF that forms when the least compressive stress normal to the borehole (horizontal in this case) (Peska and Zoback, 1995). The second DITF appears as a set of small fractures arranged in en-échelon pattern aligned with the axial DITF above it (DITF_B

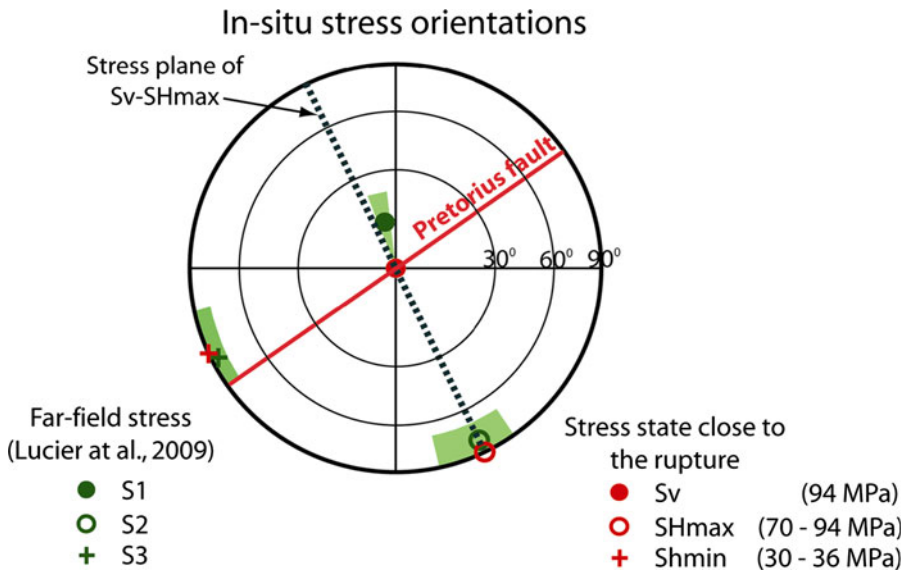

Figure 8
Stereographic projection of the principal stress axes of the far-field stress-state and their range of orientations (*green*) (from Lucier *et al.*, 2009), and the stress-state close to the M2.2 rupture-zone (*red*) (see text)

in Fig. 9b). This en-échelon appearance of the DITF indicates that the least compressive stress locally deviates, most likely by a few degrees, from normality to the borehole (Peska and Zoback, 1995). The transition between the two types of DITF occurs at a small fault that crosses the borehole (Fault C in Fig. 9b). The orientation of the two DITF in borehole #10 is 336° indicating S_{Hmax} in this direction, which is in good agreement with the S_{Hmax} deduced from the breakouts above.

We note that gaps in breakout occurrence, slight rotation of breakout orientations, and transition of DITF mode, occurs primarily where faults or bedding surfaces cross the boreholes (points D in Fig. 9a). Similar localized rotations were interpreted as indicating recent slip on the faults that perturbs the local stress field (Barton and Zoback, 1994; Lucier *et al.*, 2009). Adopting this interpretation to our observations in boreholes 10 and 13 would suggest that some of the faults and bedding planes within the NELSAM area were recently active. The occurrence of such slip is expected in the active mine, yet the slip magnitude was probably small.

The magnitudes of the in-situ stresses are determined following Zoback *et al.* (2003) who calculated the effective hoop stress ($\sigma_{\theta\theta}$) and the radial stress (σ_{rr}) at the borehole wall by using the modified Kirsch equations (Kirsch, 1898),

$$\sigma_{\theta\theta} = S_{\mathrm{hmin}} + S_{\mathrm{Hmax}} - 2(S_{\mathrm{Hmax}} - S_{\mathrm{hmin}})\cos 2\theta - 2P_{\mathrm{p}} - \Delta P - \sigma^{\Delta T}$$

$$\sigma_{rr} = \Delta P$$

$$\sigma_{zz} = S_v - 2v(S_{\mathrm{Hmax}} - S_{\mathrm{hmin}})\cos 2\theta - P_{\mathrm{p}} - \sigma^{\Delta T}$$

where S_{hmin} and S_{Hmax} are the minimum and maximum horizontal stress components, respectively, σ_{zz} the effective stress parallel to the axis of a vertical borehole, θ is the angle measured from the azimuth of S_{Hmax}, P_{p} is the pore pressure, ΔP is the difference between the pressure within the borehole and the pore pressure, v is Poisson's ratio, and $\sigma^{\Delta T}$ is the thermal stress due to the difference between the temperature inside the borehole and the formation. The thermal stress can be described by:

$$\sigma^{\Delta T} = (\alpha_t E \Delta T)/(1 - v)$$

where α_t is the thermal expansion coefficient of the formation and E is the Young's modulus (Zoback *et al.*, 2003).

The circumferential effective stress was calculated at the borehole walls for the following conditions: borehole internal pressure = 3.8 MPa

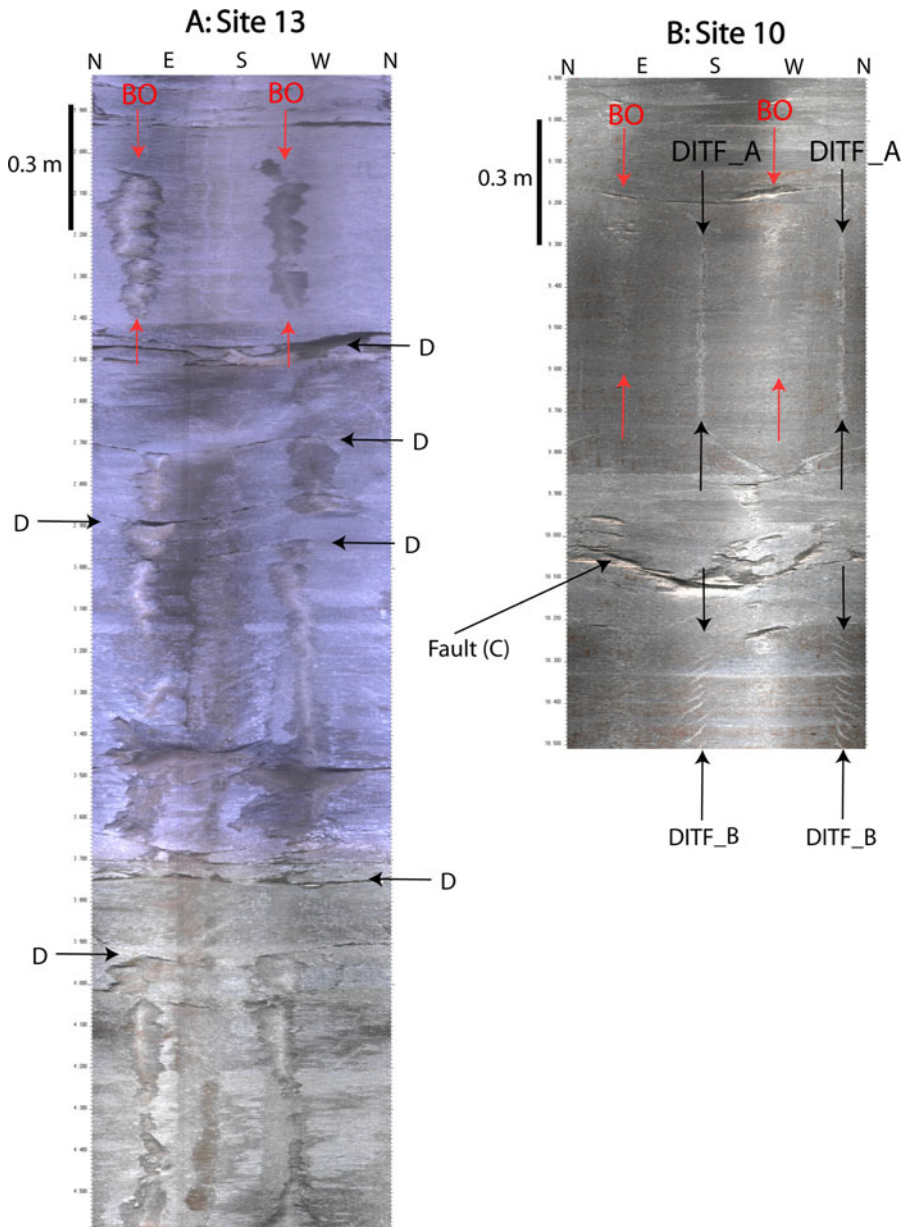

Figure 9
Image logs of two vertical boreholes close to the M2.2 rupture (locations in Fig. 6). **a** Partial image of borehole 13 with well developed breakouts (BO), some of which terminate against fault-zones and bedding surfaces (e.g., mark D). **b** Partial image of borehole 10 with poorly developed borehole breakouts (BO), well developed drilling-induced tensile fractures (marked DITF_A), and a set of short, inclined fractures at the bottom of the image (marked DITF_B) (text)

(measured water pressure); pore pressure = 0 (for the very tight quartzite); $\Delta T = 25°C$ (temperature difference between drilling water and the rock); Young's modulus = 77 GPa (rock mechanics experiments); Poisson's ratio = 0.21; $\alpha_t = 7.1 \times 10^{-6}$ (crystalline quartz); $S_V = 97$ MPa (3.6 km of overburden with a density of 2,700 kg/m^3). The magnitudes of the in-situ stresses is estimated for the section of hole 10 that includes both the DITF and the poorly developed breakouts. The calculations were done by trial-and-error of simultaneously solving for stress magnitudes that best fit the breakout width of

20° and the presence of DITF, for a reasonable range of uniaxial compressive and tensile strength of the quartzites of 190–220 and 10–30 MPa, respectively. The calculations for hole 10 suggest a maximum horizontal stress between 81 and 94 MPa, and a minimum horizontal stress between 24 and 35 MPa.

The observations of well developed breakouts in hole 13 with a width up to 40° and the lack of borehole failure within hole 9 were used to further constrain the magnitude of the stress field within the area of the M2.2 event by using the same method. The results for both hole 10 and hole 13 indicate horizontal stresses of $S_{hmin} = 30–36$ MPa and $S_{Hmax} = 70–94$ MPa (Table 3). The fact that the in-situ stresses for the two boreholes have similar orientations and fall within constrained magnitudes suggest that the in-situ stresses listed in Table 3 closely represent the local in-situ stress field within the vicinity of the M2.2 rupture. Furthermore, these in-situ stresses are similar to the far-field stress state calculated by Lucier *et al.* (2009) (Fig. 8), suggesting that perturbations of the far-field stress are small at the vicinity of the rupture.

4.2.4 Stresses on Rupture Segments

The four surfaces that were reactivated during the M2.2 event have different attitudes: 43°/167°, 20°/161°, 81°/149°, and 85°/340° for surfaces A–D, respectively (Part I, Fig. 17). While their strikes are similar to each other with average of 69° ± 7° (sub-parallel to the Pretorius fault), the inclinations of these segments vary over a 90° range. The stress plane of largest principal stresses, $S_v - S_{Hmax}$, of both local and remote stresses (Fig. 8) is vertical and trends 335°, which is almost normal to the Pretorius fault and to the A–D segments. Under this geometric relation, the ratio of shear stress/normal stress calculated for the four segments by using the in-situ stress data of Table 3 are very low, ranging from 0.05 to 0.13. Experimental (Byerlee, 1967) and field (Reches *et al.,* 1992; Sibson, 1994) analyses indicate that this stress ratio should be 0.6–0.85 for slip to occur. The effects of these low values of resolved shear stress are discussed later.

Table 3

Local in-situ stress state determined from borehole failure observed in holes 9, 10 and 13

	Magnitude (MPa)	Plunge (°)	Trend (°)
S_{Hmax}	70–94	0	335
S_{hmin}	30–36	0	245
S_v	94	90	0

5. Mechanical Analysis

5.1. Puzzling Behavior of the M2.2 Rupture

Our analysis of the structure of the M2.2 rupture-zone revealed that the slip during this event is almost exclusively localized along the contact between the quartzitic host rock and the cataclasite of pre-existing segments of the Pretorius fault (Part I). A few aspects of this localization are puzzling. First, the M2.2 reactivation occurred after ~2 Ga of inactivity of the Pretorius fault with more than ample time for cementation and strengthening of the cataclasites. As we showed experimentally, the cataclasite is currently an elastic-brittle solid that is more brittle than the surrounding host quartzitic rocks (Table 2). Second, the stress field in the mine in general, and the M2.2 rupture area in particular, is controlled by the present tectonic setting of South Africa and the mining activity. This stress field is likely to differ from the (unknown) stress state that formed the Pretorius fault ~2.7 Ga ago. Moreover, the resolved shear-stress along the reactivated segments is very low according to our in-situ stress measurements (above). Third, that slip activated four segments that significantly differ from each other in orientation (Part I, Fig. 17), origin (one principal-slip-zone, two fault segments, and one bedding surface), and amount of ancient slip (large on the principal-slip-zone). Under these conditions it is expected that failure would occur by forming new faults and will be associated with major fracturing and brecciation. None of these has happened and our analysis to explain these puzzling relations is presented below.

5.2. Mechanism of Slip Localization

5.2.1 Experimental Testing of Slip Localization

We first explore the above questions by running a specially designed rock-mechanics experiment. One section of the core collected from the DafBio

borehole drilled across the Pretorius fault (Part I) contained an undisturbed contact of cataclasite and quartzite. We use this section to prepare a large rock cylinder (diameter of 4.27 cm, and length of 12.7 cm) with the contact inclined at 33° to the long axis of the cylinder. It is important to note that in this case the cataclasite is not foliated (see discussion above of foliation effect). The sample was loaded under 60 MPa confining pressure by two cyclic stages of unloading and reloading, around 100 and 200 MPa differential stress, after which it was run to failure (Fig. 10). Failure occurred at 313 MPa differential stress, and the sample displays strain hardening before failure is reached. Inspection of the failed sample revealed distinct zone of white, 'rock-flour' along the quartzite-cataclasite contact (Fig. 11). The thin-sections across the failed sample showed that the main fault developed along the quartzite-cataclasite contact, with multiple secondary fractures which branch into the quartzitic side and are generally sub-parallel to the sample axis (Fig. 11c, d). It is evident that highly asymmetric damage exists between the quartzite and the cataclasite. Intense off-fault damage occurred within the quartzite in the form of these secondary, axial fractures whose density reduces with distance from the contact. Commonly, these axial fractures die off within individual quartz grains (close-ups of Fig. 11c, d). Close to the contact with the cataclasite, the highly dense fractures in the quartzite coalesce to form a through going fault. On the other hand, the cataclasite, whose strength is about one half of the quartzite's strength, remains visually undamaged (Fig. 11).

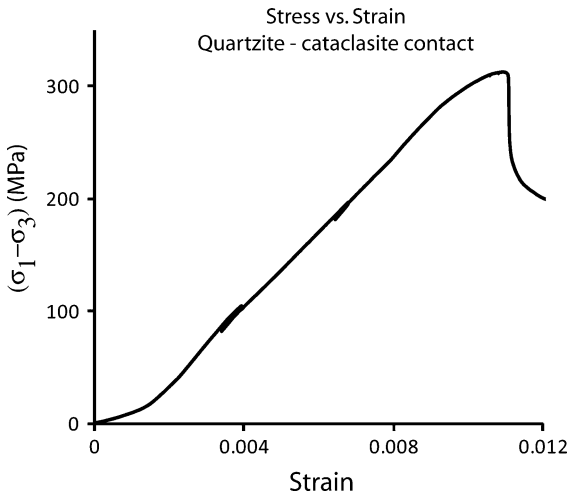

Figure 10
Stress–strain curve for a rock sample containing the cataclasite–quartzite contact of the Pretorius fault-zone. The experiment was conducted under confining stress of 60 MPa. Failure occurred at a differential stress of 313 MPa after the sample experienced two cyclic stages of unloading and reloading, around 100 and 200 MPa differential stress. The sample displays strain hardening before failure

These experimental observations are strikingly similar to the observations in the M2.2 rupture-zone in two main points:

1. Both the experiment and the M2.2 rupture-zone are characterized by slip that is localized along the quartzite-cataclasite contact; compare Figs. 19–20 of Part I with Fig. 11 here.
2. Both the experiments and the M2.2 rupture-zone display a zone of white, rock-flour gouge along the slipping surface (Part I, Figs. 19–20, 11a). This experimental observation confirms the use of this white gouge as indicator of shear failure in South African mines (McGarr *et al.,* 1975).

5.2.2 *Hypothesis: Slip Localization Controlled by Mechanical Heterogeneity*

Following the above experimental results (Fig. 11), we hypothesize that slip localization in the M2.2 event and the experiment is controlled by similar failure mechanisms that are related to the contrast of mechanical properties between the cataclasite and the quartzite. Our rock mechanics experiments revealed profound differences in the mechanical properties of the quartzitic host rocks and the cataclasite (Table 2) (Figs. 1, 3) even though the two rock types have the same mineralogical compositions. We hypothesize that this mechanical heterogeneity localized the M2.2 rupture along preexisting segments rather than generating new faults. We quantitatively explore this hypothesis by finite-element simulations presented below.

5.2.3 *Finite-Element Simulations*

Model Structure We use the Abaqus finite-element code to analyze an idealized 2D model of a pre-existing fault-zone in a medium (Fig. 12). The fault-

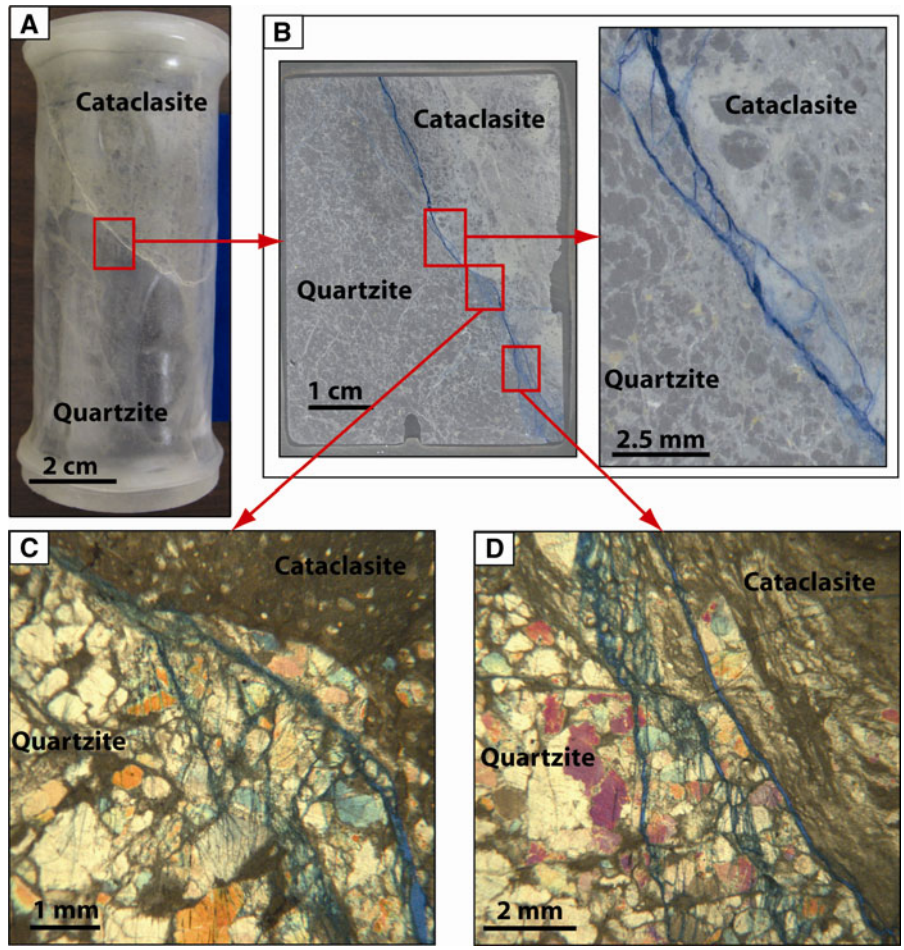

Figure 11
Experimental results of a rock-mechanics failure experiment with a sample with initially unfractured quartzite–cataclasite contact; run under 60 MPa confining pressure; sample is 12.7 cm tall and 4.27 cm in diameter. **a** The sample after failure; note white rock-flour zone along the quartzite–cataclasite contact. **b** Thin section (oversized, non standard thickness) views of the main fault (blue epoxy) along the contact. Note multiple branches that form a few mm thick zone. **c**, **d** Close-up of fault branches with significant off-fault damage in the quartzite. Axial fractures within the quartz grains significantly increase towards the contact and link up to eventually form the main fault

zone is represented by a thin elongated elliptical inclusion with an aspect ratio of 1:50 that is embedded in a medium of 100 × 100 m; the ellipse's long axis is oriented 45° to the *x*-axis (Fig. 12a). The material properties assigned to the ellipse and medium are the mechanical properties derived from the rock-mechanics experiments on the cataclasite and host quartzite of the Pretorius fault, respectively. The ellipse is modeled by an isotropic, linear elastic material with $E = 77$ GPa and $\nu = 0.23$. The medium is modeled as strain-hardening elastic–plastic solid with isotropic elastic component and isotropic plastic strain-hardening component. Yield strength and the corresponding plastic strain values are empirically determined from the experimental stress–strain curve of the host quartzite. The post-peak stress-drop of the quartzite (Fig. 3) is replaced here by perfect plasticity at differential stress of 350 MPa.

We ran the simulations with Abaqus/CAE Standard solver (Student edition V 6.7). The model is constructed of three-node linear plane-strain triangular mesh with reduced mesh size towards the tips of the elliptical inclusion (Fig. 12a).

Simulation Results The model was loaded by arbitrary plane-strain displacement on the model's

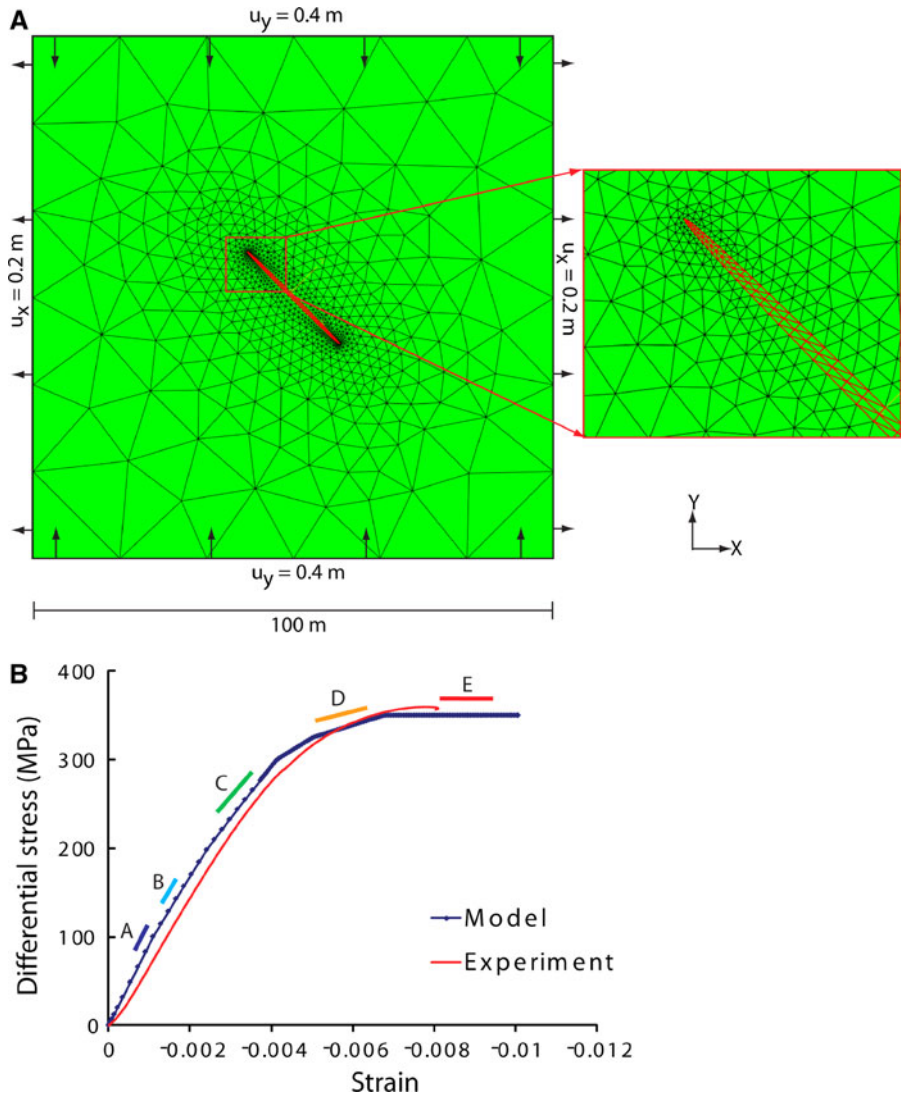

Figure 12

Plane-strain, finite-element model with elliptical inclusion of an idealized fault. **a** Model geometry with elongated inclusion oriented 45° to *x*-axis. The three-node linear plane-strain triangular mesh is refined towards the ellipse and towards the tips of the ellipse. Applied boundary displacements are 0.8% shortening in the *x*-direction and 0.4% extension in the *y*-direction. **b** Stress–strain curve of an element away from the ellipse (*blue*), and experimental rock-mechanics curve of sample NEL08 (*red*). Also plotted is the stress-state for each of the A–E groups during the simulation (see text and Fig. 14)

edges with 0.8 m shortening in the y-direction and 0.4 m extension in the *x*-direction. These values correspond to a total applied shear strain of 0.006 parallel to the inclusion. These boundary displacements were applied in 100,000 equal incremental steps. The quality of the rheology simulation is demonstrated by comparing the stress–strain curves of the rock mechanics experiments (quartzite) and model (medium) (Fig. 12b).

Calculated strain maps are shown in Fig. 13. These are maps of the plastic-shear-strain parallel to the inclusion; this component is about equal to maximum plastic-shear-strain in the model as the inclusion is initially at 45° to *x* axis. The maps show the following features: (1) the inclusion-parallel plastic-shear-strain away from the inclusion is about 0.008 in the final stage; (2) systematic increase of plastic-shear-strain with progressive displacement

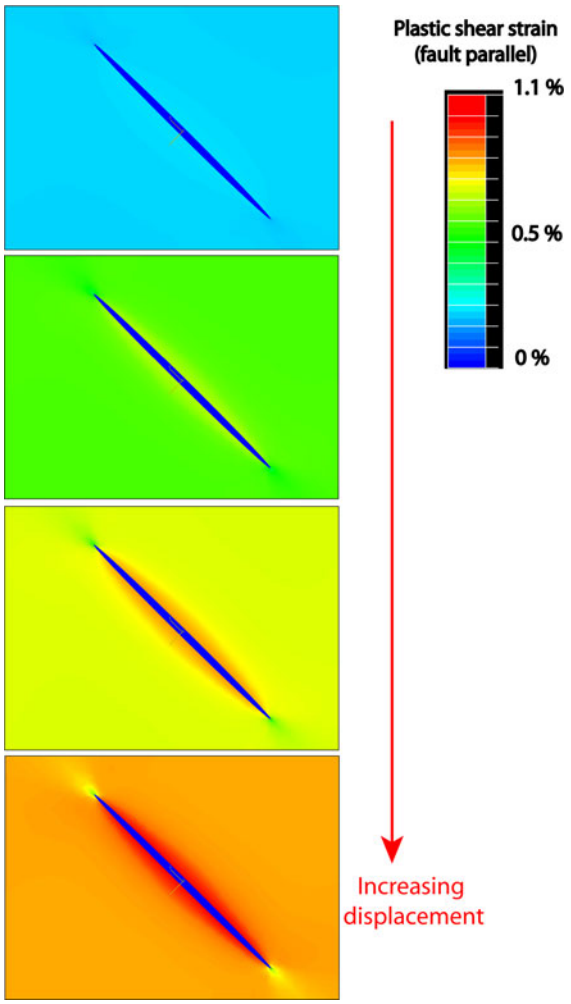

Figure 13
Maps of the plastic-shear-strain that is parallel to inclusion, as it develops with increasing displacement. Note that the plastic-shear-strain increases towards the inclusion reaching values of 1.1×10^{-2} at the contact

increments; (3) a zone of increased plastic-shear-strain along the inclusion-medium contact; (4) no plastic strain in the elastic inclusion, as expected; and (5) zones of relative reduced plastic-shear-strain close to the tips of the elliptical inclusion, which is unexpected. Immediate implications of these results are that failure is likely to occur at the inclusion-medium contact, and that failure is less likely to occur at the inclusion tips.

The plastic-shear-strain distribution in the medium is further plotted along a profile normal to the inclusion (F–F′ in inset of Fig. 14). Figure 14 displays curves of the difference between the local fault-parallel plastic-shear-strain, $\varepsilon_{ps(total)}$, and the same strain component in the medium away from the inclusion $\varepsilon_{ps(medium)}$ (point F). The ten curves in Fig. 14 represent ten progressive stages in the deformation separated by 10% of the total boundary displacements. We recognize five stages of the deformation progress, marked A–E. The von-Mises stress associated with each of these stages in one element at the edge of the inclusion is marked on Fig. 12b. Our experimental work revealed that strain-hardening of the quartzite is associated with distributed damage primarily by axial micro-fracturing (Fig. 11), which intensifies before the macroscopic failure. Using these observations, we interpret the stages A–E of Figs. 12b, 14 as corresponding to the following physical processes in the quartzite:

1. The linear-elastic behavior of the medium without the onset of damage (plastic strain).
2. Initiation of damage with minor localization of plastic-shear-strain at the edge of the ellipse, coinciding with stable growth of micro-fractures.
3. Increase of damage and strain hardening, during which micro-fractures grow to develop axial fractures, causing dilation of the quartzite.
4. Acceleration of damage formation by unstable crack growth, close to failure. Most of the strain localization occurs during this stage (Fig. 14a).
5. Post-peak stage that is defined by perfect plasticity in the simulation (Fig. 12b), and corresponds to shear localization along the quartzite-cataclasite contact (Fig. 11).

Summary of the Simulation Results The objective of the present simulations is to understand the failure of the Pretorius fault during the M2.2 earthquake. In the Pretorius fault-zone, the medium is the host quartzite with strain-hardening plastic rheology, with zones of brittle-elastic cataclasite (inclusion). The mining activity that preceded the M2.2 event deformed the fault-zone in the eventual rupture area and beyond. In the simulation, this deformation is represented by the boundary displacements. The simulation reveals two central features that can be applied to the M2.2 rupture in the mine: (1) The presence of an inclusion with different mechanical properties generates significant strain localization

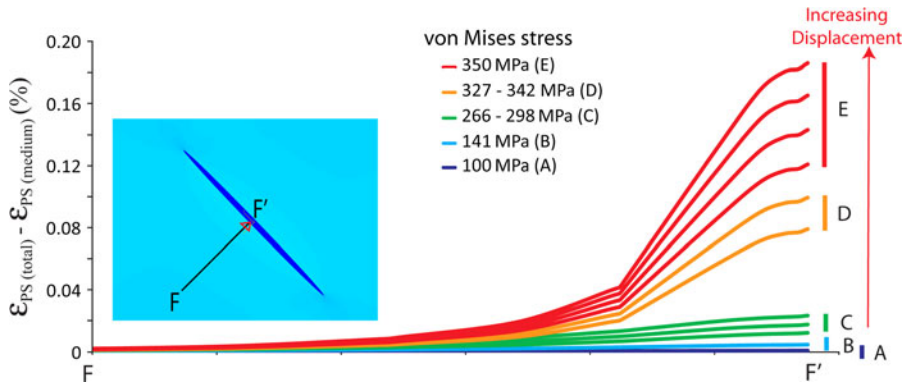

Figure 14
Distribution of plastic-shear-strain in the medium along profile F–F′ (*inset*) as a function of progressive boundary displacements. Curves of the difference between the inclusion-parallel plastic-shear-strain, $\varepsilon_{ps(total)}$, and $\varepsilon_{ps(medium)}$, the same strain component in the medium away from the inclusion. The *individual lines* represent 10,000 displacement increments each, and are divide into five groups A–E (Fig. 12b)

along the contact between the medium and the inclusion (Fig. 14); and (2) The medium at the proximity of the inclusion tips acquire relatively low strain concentration. This strain distribution is the opposite of the well-known solutions for dislocations (or faults) in which the largest strain amplification is localized close to the dislocation tips (e.g., Reches and Lockner, 1994). The implications of these results to the M2.2 event are discussed below.

6. Discussion

6.1. Slip Along Unfavorable Oriented Fault Segments

The local in-situ stress field in the vicinity of the exposed rupture was determined from failure features in three boreholes drilled about 1 year after the M2.2 event of December 12, 2004. The analysis revealed a relatively uniform homogeneous stress state (Table 3), which is consistent with the far field in-situ stress (Lucier *et al.*, 2009) (Fig. 8). Therefore, we conclude that the determined in-situ stresses of Table 3 represent the state of stress in the vicinity of the M2.2 event. The above conclusion leads to another puzzle (above). The S_v–S_{Hmax} plane is roughly perpendicular to the reactivated segments (Fig. 8), resulting in very low ratio of shear stress/normal stress with maximum value of 0.13 (above). It is puzzling how slip could occur simultaneously along four segments, none of which is in a favorable orientation. We consider a few mechanisms that could explain this anomaly:

6.1.1 Quasi-Static Weakening

Similar configurations to our observations have been determined close to large, mature faults. For example, the San Andreas Fault, California, where S_{Hmax} is at high angle (60°–80°) with respect to active sub-vertical strike slip faults (Zoback *et al.*, 1987), and the active Nojima Fault, Japan, where stress measurements suggests that S_{Hmax} is oriented almost perpendicular to the active fault trend (Yamamoto *et al.*, 2000). These observations can be explained, for example, by elevated pore fluid pressure in a mature, clay rich fault-zone (Rice, 1992; Byerlee, 1993; Tembe *et al.*, 2009). However, these explanations are not applicable to the strong Pretorius fault which is drained by the mining activity.

6.1.2 Dynamic Weakening

It was shown experimentally that the shear resistance of a fault may be significantly lower during high velocity, co-seismic slip rates (Tsutsumi and Shimamoto, 1997; Di Toro and Pennacchioni, 2004; Reches and Lockner, 2010). While dynamic weakening is commonly used to explain earthquake instability, it is generally believed that slip initiates when the in-situ stresses exceed the high static friction of rocks.

6.1.3 Stress Rotation Within a Damage Zone

Faulkner *et al.* (2006) and Healy (2008) analyzed stress rotations near faults due to the presence of a damage zone. They showed that the reduction of the elastic properties and preferred crack orientations could rotate the maximum compressive stress by as much as 45°. Our stress measurements are conducted within three boreholes that are 60 m or less from the rupture-zone; thus, if stress rotation exists, it is restricted to the Pretorius fault-zone which is tens of meters wide. The elastic properties of the quartzite within the Pretorius fault-zone are $E = 77$ GPa (Young modulus) and $\nu = 0.21$ (Poisson ratio) (Tables 1, 2), and the elastic properties of Witwatersrand quartzite measured elsewhere in South African mines are $E = 80$ GPa and $\nu = 0.19$ (e.g., Gay, 1976). We think that if the rocks in TauTona mine away from the Pretorius fault have elastic properties similar to the regional values, than the estimated modulus reduction (3 out of 80 GPa) is too small to cause appreciable stress rotation.

6.1.4 Earthquake Dynamic Stress Field

If a local, small slip occurred within a weak area in the Pretorius fault, it could dynamically alter the stress field and allow the M2.2 to slip in unfavorable static stress state. This initial small event could serve as a trigger to a much larger event. A possible scenario was presented by Boettcher *et al.* (2009) in their analysis of small earthquake in the Pretorius fault. They show that two pre-shocks of $M = -3.9$ and $M = -3.4$ preceded an $M = -2.7$ main-shock by a few tens of milliseconds. One may speculate that similar pre-shocks could activate slip along unfavorable surfaces during the M2.2 earthquake.

6.1.5 Mechanical Heterogeneity

Our preferred explanation was discussed earlier and briefly mentioned here. The pre-event mining activity loaded the Pretorius fault-zone, and due to the mechanical heterogeneity, the quartzite zones along the cataclasite zones were intensely plastically strained with respect to the bulk strain in the fault-zone. When slip initiates at an arbitrary weak point, the failure would propagate preferentially along the highly strained, highly stressed zones at the quartzite-cataclasite contacts. We argue that this failure of pre-stressed zones is controlled more by the mechanical heterogeneity and less by the in-situ stress distribution or frictional values.

7. Conclusions

The Pretorius fault, TauTona mine, South Africa, is a $\sim$10 km long, oblique strike slip fault with oblique displacement of up to 200 m. We identified three structural zones within the Pretorius fault-zone (Part I): (1) an outer damage zone, $\sim$100 m wide, of brittle deformation manifested by multiple widely spaced fractures and faults with slip up to 3 m. (2) A inner damage zone, 25–30 m wide, with high density of anastomosing conjugate sets of fault segments and fractures, many of which carry cataclasite zones. (3) A single, dominant segment, with a cataclasite zone up to 50 cm thick, is the principal slip zone that accommodated most of the slip of the Pretorius fault. This fault-zone structure indicates that during its Archaean activity, the Pretorius fault has passed the stage of fault-zone immaturity and entered the stage of slip localization with multiple events along a single principal slip zone.

Reactivation of the Pretorius fault occurred during the 2004 M2.2 event. Our analysis of the rupture-zone shows that (Part I) (1) slip occurred almost exclusively along four, pre-existing large, quasi-planer segments of the ancient fault-zone; (2) the slipping segments contain brittle cataclasite zones up to 0.5 m thick; (3) these segments are not parallel to each other; (4) gouge zones, 1–5 mm thick, composed of white 'rock-flour' formed almost exclusively along the cataclasite-host rock contacts of the slipping segments; (5) locally, new, fresh fractures branched from the slipping segments and propagated in mixed shear-tensile mode; (6) the maximum observed shear displacement is 25 mm in oblique-normal slip.

The Pretorius fault, including its ancient gouge zones, was re-cemented and sintered over 2 Ga and regained strength. Our rock mechanics testing indicated that the brittle cataclasite zones are embedded

in damaged, elastic–plastic quartzites that undergo strain-hardening and volumetric expansion during loading. This mechanical contrast represents the heterogeneous nature of the Pretorius fault. Further, the local in-situ stress state, which we determined, is not favorable to slip along the reactivated segments. Thus, this fault-zone is expected to fail like an intact rock body that ignores the internal fault-zone structure. Our finite-element modeling, which used actual properties of the Pretorius fault-rocks, indicates that the slip is likely to reactivate the ancient cataclasite-bearing segments, as observed, due to the strong mechanical contrast between the cataclasite and the host quartzitic rock, and not due to weakness zonation.

Acknowledgments

We are in debt to many people and organizations. Foremost to Gerrie van Aswegen of ISS International who guided and advised us throughout this entire study. This work was not possible without the invaluable help and support by Hannes Moller, Pieter van Zyl, Rob Burnet, and many other workers in TauTona mine and ISSI. We greatly appreciate the help in underground work by Tom Dewers, Amir Allam, Kate Moore, and Matthew Zechmeister of University of Oklahoma, Reginald Domoney, Selwyn Adams, and Curnell Campher, of the University of Western Cape, South Africa, Amie Lucier of Stanford University, and Malcolm Johnston, US Geological Survey. This work could not be completed without the important advice, suggestions and encouragement by the NELSAM team of Tom Jordan, Malcolm Johnston, Mark Zoback, TC Onstott, as well as Hiroshi Ogasawara, Ritsumeikan University, Japan, and Uli Harms, GFZ, Germany. Many thanks to AngloGoldAshanti for the permission to work in the TauTona mine and the generous logistic support. The thoughtful comments of two anonymous reviewers significantly improved the manuscript. This work was supported by the National Science Foundation under Grant no. 0409605 (NELSAM project), and the drilling grant by ICDP (DAFSAM project). Other sponsors of this work include US Geological survey, AngloGoldAshanti, ISS International, and National Research Foundation (NRF).

References

Armstrong, R.A., Compston, W., Retief, E.A., Williams, I.S., and Welke, H.J. (1991), *Zircon ion microprobe studies bearing on the age and evolution of the Witwatersrand triad*, Precambrian Res., *53*, 243–266.

Barton, C.A., and Zoback, M.D. (1994), *Stress perturbations associated with active faults penetrated by boreholes: possible evidence for near-complete stress drop and a new technique for stress magnitude measurement*, J. Geophys. Res. *99*, 9373–9390.

Boettcher, M.S., McGarr, A., and Johnston, M. (2009), *Extension of Gutenberg–Richter distribution to M_w −1.3, no lower limit in sight*, Geophys. Res. Lett., *36*.

Byerlee, J.D. (1967), *Frictional characteristics of granite under high confining pressure*, J. Geophys. Res. *72*, 3639–3648.

Byerlee, J. (1993), *Model for episodic high-pressure water in fault zones before earthquakes*, Geology, *21*, 303–306.

Cartwright, P., and Walker, G. (2000), In-situ stress measurement, 83 level shaft pillar area, TauTona mine, AngloGold.

Cook, N.G.W., (1963), The seismic location of rockbursts, In: Proc. Rock Mechanics Symposium, 5th, Pergamon Press, Oxford, p. 493.

Di Toro, G., and Pennacchioni, G. (2004), *Superheated friction-induced melts in zoned pseudotachylytes within the Adamello tonalites (Italian Southern Alps)*, J. Structural Geol., *26*, 1783–1801.

Dor, O., Reches, Z., and van Aswegen, G. (2001), Fault zones associated with the Matjhabeng earthquake 1999, South Africa: Rockburst and Seismicity in Mines, RaSiM5 (Proceedings), South African Inst. Mining and Metallurgy, pp 109–112.

Faulkner, D.R., Mitchell, T.M., Healy, D., and Heap, M.J. (2006), *Slip on "weak" faults by the rotation of regional stress in the fracture damage zone*, Nature, *444*, 922–925.

Gay N.C. (1976), *Fracture growth around openings in large blocks of rock subjected to uniaxial and biaxial compression*. Int. J. Rock Mech. Min. Sci. & Geomech. Abstr. *13*, 231–243.

Gay N.C., and Ortlepp W.D. (1979), *Anatomy of a mining-induced fault zone*, Bull. geol. Soc. Am. *90*, 47–58.

Gibowicz, S.J., and Kijko, A. (1994), An Introduction to Mining Seismology, Academic Press, San Diego.

Gibson, R.L., Reimold, W.U., Phillips, D., and Layer, P.W. (2000), *Ar^{40}/Ar^{39} constraints on the age of metamorphism in the Witwatersrand Supergroup, Vredefort Dome (South Africa)*, South African J. Geol., *103*, 175–190.

Healy, D. (2008), *Damage patterns, stress rotations and pore fluid pressures in strike-slip fault zones*, J. Geophys. Res., *113*.

Heesakkers, V., Murphy, S., Lockner, D.A., and Reches, Z., (2011) (Part I). Earthquake Rupture at Focal Depth, Part I: structure and rupture of the Pretorius Fault, TauTona Mine, South Africa (this volume).

Katz, O., Gilbert, M.C., Reches, Z., and Roegiers, J.C. (2001), *Mechanical properties of the Mount Scott Granite, Wichita Mountains, Oklahoma*, Oklahoma Geology Notes, *61*, 28–34.

Katz, O., and Reches, Z. (2004), *Microfracturing, damage, and failure of brittle granites*, J. Geophys. Res., *109*, B1, B01206.

KIRSCH, G. (1898), *Die Theorie der Elastizitat und die Bedurfnisse der Festigkeitslehre*. VDI Z, *42*, 707.

LOCKNER, D.A. (1998), *A generalized law for brittle deformation of Westerly granite*, J. Geophys. Res., *103*, 5107–5123.

LUCIER, A.M., ZOBACK, M.D., HEESAKKERS, V., RECHES, Z., and MURPHY, S.K. (2009), *Constraining the far-field in situ stress state near a deep South African gold mine*, Int. J. Rock Mechanics Mining Sci., *46*, 555–567.

MCGARR, A., (1984), Some applications of seismic source mechanism studies to assessing underground hazard: Rockburst and Seismicity in Mines, In: Symp. Ser. No. 6, South African. Inst. Min. Metal., (ed Gay, N.C. and Wainwright, E.H.), Johannesburg, 199–208.

MCGARR, A. (1992), *Moment tensors of ten Witwatersrand mine tremors*, Pure Appl. Geophys., *139*, 781–800.

MCGARR, A. (2002), *Control of strong ground motion of mining-induced earthquakes by the strength of the seismogenic rock mass*. J. the South African Inst. Mining Metallurgy. *102*, 225–229.

MCGARR, A., and GAY, N.C. (1978), *State of Stress in the Earth's Crust*, Ann. Rev. Earth Planetary Sci., *6*, 405–436.

MCGARR, A., POLLARD, D.D., GAY, N.C., and ORTLEPP, W.D. (1979a), Observations and Analysis of Structures in Exhumed Mine-induces Faults, Proceedings of Conference VIII: Analysis of Actual Fault Zones in Bedrock, US Geol. Survey, Menlo Park, Open file Rep. 79–1239, 101–120.

MCGARR, A., SPOTTISWOODE, S.M., GAY, N.C., and ORTLEPP, W.D. (1979b), *Observations relevant to seismic driving stress, stress drop, and efficiency*, J. Geophys. Res., *84*, B5, 2251–2261.

MCGARR, A., SPOTTISWOODE, S.M., and GAY, N.C., (1975), *Relationship of mine tremors to induced stresses and to rock properties in the focal region*, Bull. Seism. Soc. Am., *65*, 981–993.

MENDECKI, A.J., Seismic Monitoring in Mines, (ed. MENDECKI, A.J.) (Chapman and Hall, London 1997).

OGASAWARA, H., T. YANAGIDANI, and M. ANDO (editors), (2002), Seismogenic Process Monitoring, Balkema, Rotterdam.

ORTLEPP W.D. (1978), The mechanism of a rockburst, Proc. 19th U.S. Rock Mechanics Symp., Reno, Nevada, 476–483.

PESKA, P., and ZOBACK, M.D. (1995), *Compressive and tensile failure of inclined well bores and determination of in situ stress and rock strength*, J. Geophys. Res., *100*, 12791–12811.

RECHES, Z. (1979), *Deformation of a foliated medium*, Tectonophysics, *57*, 119–129.

RECHES, Z. (2006), *Building a natural earthquake laboratory at focal depth*, Scientific Drilling *3*, 30–33.

RECHES, Z., BAER, G., AND HATZOR, Y. (1992), *Constraints on the Strength of the Upper Crust from Stress Inversion of Fault Slip Data*, J. Geophys. Res., *97*(B9), 12481–12493.

RECHES, Z., and ITO, H., Scientific drilling of active faults: past and future, In Scientific Drillings Continental Scientific Drilling A Decade of Progress, and Challenges for the Future (ed. HARMS, U., KOEBERL, C., and ZOBACK, M.D.) (Springer 2007), 235–258.

RECHES, Z., and LOCKNER, D.A. (1994), *Nucleation and growth of faults in brittle rocks*, J. Geophys. Res., *99*, 18159–18173.

Reches, Z., and LOCKNER, D.A. (2010). *Fault weakening and earthquake instability by powder lubrication*, Nature, *467*, 452–456.

RICE, J.R. (1992), Fault stress states, pore pressure distributions, and the weakness of the San Andreas Fault, In Fault mechanics and transport properties of rock (ed. Evans, B., and W. Tf), London, Academic press, pp. 475–504.

RICHARDSON, E., and JORDAN, T.H. (2002), *Seismicity in Deep Gold Mines of South Africa: Implications for Tectonic Earthquakes*, Bull. Seism. Soc. Am., *92*, 1766–1782.

ROBB, L.J., CHARLESWORTH, E.G., DRENNAN, G.R., GIBSON, R.L., and TONGU, E.L. (1997), *Tectono-metamorphic setting and paragenetic sequence of Au-U mineralisation in the Archaean Witwatersrand Basin, South Africa*, Australian J. Earth Sci., *44*, 353–371.

SIBSON, R.H. (1994), *Crustal stress, faulting and fluid flow: geological Society*, London, Special Publications, *78*, 69–84.

SPOTTISWOODE, S.M. (1980), Source mechanism studies on Witwatersrand seismic events, Ph.D Thesis, University of the Witwatersrand, Johannesburg.

SPOTTISWOODE, S.M., and MCGARR, A. (1975), *Source parameters of tremors in a deep-level gold mine*, Bull. Seism. Soc. Am., *65*, 93–112.

TEMBE, S., LOCKNER, D., and WONG, T.F. (2009), *Constraints on the stress state of the San Andreas Fault with analysis based on core and cuttings from San Andreas Fault Observatory at Depth (SAFOD) drilling phases 1 and 2*, J. Geophys. Res., *114*.

TSUTSUMI, A., and SHIMAMOTO, T. (1997), *High-velocity Frictional Properties of Gabbro*, Geophys. Res. Lett., *24*.

VAN ASWEGEN, G., RECHES, Z., JORDAN, T.H., and BEN-ZION, Y. (2002), Drilling Active Faults in South Africa Mines: An in-situ laboratory to study earthquake and fault mechanics, Am. Geophy. Union, Fall Meeting 2002, Abstract U72B-0021.

YABE, Y., PHILIPP, J., NAKATANI, M., MOREMA G., NAOI, M., KAWAKATA, H., IGARASHI, T., DRESEN, G., OGASAWARA, H., and JAGUARS, (2009), *Observation of numerous aftershocks of an Mw 1.9 earthquake with an AE network installed in a deep gold mine in South Africa*. Earth Planets Space, *61*, e49–e52.

YAMAMOTO, K., SATO, N., and YABE, Y. (2000), Stress state around the Nojima fault estimated from core measurements, Proceedings of the Int. Workshop on the Nojima Fault Core and Borehole Data Analysis, 239–246.

ZOBACK, M.D., BARTON, C.A., BRUDY, M., CASTILLO, D.A., FINKBEINER, T., GROLLIMUND, B.R., MOOS, D.B., PESKA, P., WARD, C.D., WIPRUT, D.J., and HUDSON, J.A. (2003), *Determination of stress orientation and magnitude in deep wells*, Int. J. Rock Mechanics and Mining Sci., *40*, 1049–1076.

ZOBACK, M.D., ZOBACK, M.L., MOUNT, V.S., SUPPE, J., EATON, J.P., HEALY, J.H., OPPENHEIMER, D.H., REASENBERG, P.A., JONES, L.M., RALEIGH, C.B., WONG, I.G., SCOTTI, O., and WENTWORTH, C.M. (1987), *New evidence on the state of stress of the San Andreas fault system*, Science, *238*, 1105–1111.

(Received July 23, 2010, revised May 21, 2011, accepted May 23, 2011, Published online August 9, 2011)